Considerable improved near-infrared luminescence in ionic-free doped $ZnAl_2O_4$ by oxygen defects engineering

Huan Yang[1], Junqing Xiahou[1], Qi Zhu[1*], and Ji-Guang Li[2]

[1]*Key Laboratory for Anisotropy and Texture of Materials (Ministry of Education), School of Materials Science and Engineering, Northeastern University, Shenyang, Liaoning 110819, PR China*

[2]*Research Center for Functional Materials, National Institute for Materials Science, Namiki 1-1, Tsukuba, Ibaraki 305-0044, Japan*

*Corresponding author

Dr. Qi Zhu

Tel: +86-24-8367-2700

E-mail: zhuq@smm.neu.edu.cn

Abstract:

Recently, the phosphor for near-infrared LED is of importance, and a lot of the researches have been attracted on the synthesis and composition design. However, the large number of researches for near-infrared luminescent materials mainly focus on activator ions doped inorganic materials, including rare earth ions and transition metal ions. Here, an ionic-free doped NIR phosphor of $ZnAl_2O_4$ is proposed for NIR LED through oxygen defects engineering. The spinel-structured $ZnAl_2O_4$ phosphors with deficiency of zinc were synthesized by high temperature solid state reaction, which were characterized by a series of techniques, including XRD, UV-Vis, XPS, EPR, DFT calculation, PLE/PL spectroscopy, and temperature-dependent PL spectra analysis. The deficiency of zinc results in the appearance of zinc vacancy (V_{Zn}) and oxygen vacancy (V_O). Most of the oxygen vacancy is V_O^+, along with a small content of V_O^{++} in $ZnAl_2O_4$. Under the excitation of ultraviolet light at 302 nm, the phosphor outputs a broad near-infrared emission band with the maximum at 715 nm. Higher concentration of zinc deficiency leads to stronger near-infrared luminescence, because of the increased oxygen vacancy. The phosphors exhibited a good thermal stability, and they were successfully packaged on the 285-nm UV LED chip, which outputted bright and intense near-infrared light, indicating that the NIR phosphors synthesized in this work have the prospect application in NIR LED.

Key Words: $ZnAl_2O_4$; near-infrared; luminescence; oxygen defects; NIR LED

1. Introduction

Light emitting diode (LED) is a kind of semiconductor electronic component that uses low-voltage direct current to generate light [1]. Compared with traditional light sources such as tungsten filament lamp and halogen lamp, LED has become a new lighting source because of its long service life, high conversion efficiency, and small volume, so it has been widely concerned [2]. In the early days, LED was generally used in display screen [3]. Recently, LED has been extended to backlight module, textile, lighting and other fields [1,4,5]. As a new emitting light source, near-infrared LED has a broad application prospect [2,6-8]. With the rapid development of science and technology, people's demand for LED light sources is not limited to the range of visible light, and began to explore new LED light sources beyond the range of visible light to the naked eye [9]. The near infrared LED is one of them. A large number of studies have shown that near-infrared LED lighting sources can be applied in many fields, such as plant lighting, bioengineering, medical imaging and so on [10-12], and have made indelible contributions to the development of human science and technology. Therefore, the phosphor for near-infrared LED is of importance, and a lot of the researches have been attracted on the synthesis and composition design.

In recent years, a large number of near-infrared rare earth luminescent materials [13] have been synthesized, which can be roughly divided into two categories: rare earth ion organic compounds and rare earth ion doped inorganic materials. Trivalent lanthanide (Ln^{3+}) ions, such as Nd^{3+}, Yb^{3+}, Pr^{3+}, Sm^{3+}, have been selected as activator ions for NIR emission [14-16]. However, the phosphors activated by Ln^{3+} ions usually have the problem of narrow spectrum and low absorptivity, because the odd and even selection of Ln^{3+} ions prohibits the 4f transition [17]. Moreover, the excessive use of rare earth metals will cause great harm and irreversibility to the environment. To solve this problem, a large number of studies have been carried out on transition metal elements for near-infrared luminescent materials, among which Cr^{3+} ions as a good activator of near-infrared phosphors have attracted extensive attention [18,19]. It is reported that in many related studies of near-infrared phosphors with Cr^{3+} ions as the

light-emitting center, the interaction between defects and Cr^{3+} was mainly discussed [20,21]. The defects can not only affect the luminous intensity of phosphors, but also be used to adjust the emission wavelength of phosphors [22,23]. However, most of these phosphors with defects are long persistent luminescence materials, with a complex composition. Their luminescent properties are affected by many factors and are not easy to adjust, and their development in the field of real-time luminescence is limited. Therefore, developing the near-infrared phosphor with defect as the sole luminous center has become a matter of concern. Defects are often considered as a disadvantage of inorganic materials because they may significantly reduce their physical and chemical properties (optical, magnetic, electrical, etc.) [24-26]. In order to obtain higher quality luminescent materials, minimizing the number of internal and external defects has become the main goal. However, defects are not always harmful, and sometimes have a positive impact on material properties [27,28]. More and more evidences show that some special types of defects, such as vacancies and impurities, will also lead to different emission characteristics of phosphors in some cases [29,30].

Zinc aluminate ($ZnAl_2O_4$) is considered as a functional material in the main luminescence applications because of its wide band gap energy, high chemical and thermal stability, good cationic dispersion and unique crystal structure [31-33]. $ZnAl_2O_4$ is an aluminate with the spinel structure, belonging to Fd-3m space group, with cubic structure and wide band gap energy (3.8 eV) [34]. The chemical formula is generally expressed as AB_2O_4, where A represents divalent metal cations, occupying tetrahedral positions, and tetrahedral gaps are formed by four oxygen ions, B represents trivalent cations, occupying octahedral positions, and octahedral gaps are formed by six oxygen ions [35]. At present, most of the studies on $ZnAl_2O_4$ are focused on the role of activator ions such as Mn^{2+} and Cr^{3+} in $ZnAl_2O_4$, while rather few studies focus on the $ZnAl_2O_4$ matrix [36-39]. It is reported that $ZnAl_2O_4$ contains many types of defects, such as V_O^+, V_O^{2+}, V_O^0, V_{Zn}^-, V_{Zn}^{2-}, O^{2-}, V_{Al}^{3-} [29]. The theoretical calculation of various defects in $ZnAl_2O_4$ shows that the formation probability of anti defects is the lowest [33], therefore, the anti site defects of Al_{Zn} will be ignored. However, through the first principle calculation, the researchers found that

the different types of defects in $ZnAl_2O_4$ would possible lead to the emission of light with different wavelengths, while the existence of oxygen vacancy defects may lead to the generation of near-infrared light. In this work, an ionic-free doped NIR phosphor of $ZnAl_2O_4$ is proposed for NIR LED through oxygen defects engineering. The spinel-structured $ZnAl_2O_4$ phosphors with deficiency of zinc were synthesized by high temperature solid state reaction, which were characterized by a series of techniques, including XRD, UV-Vis, XPS, EPR, DFT calculation, PLE/PL spectroscopy, and temperature-dependent PL spectra analysis. The outcomes in this work may pave a new way to promote the development of near-infrared luminescence and play a demonstration role on near-infrared phosphors.

2. Experiment section

2.1. Sample preparation

$ZnAl_2O_4$ and $Zn_{1-x}Al_2O_4$ (x=0-0.13) phosphors were synthesized by a high temperature solid-state reaction. Al_2O_3 (99.99%) and ZnO (99.99%) were used as raw materials. The sources were purchased from China pharmaceutical group chemical reagent Co. LTD (Shanghai, China). Based on the composition, the above materials were weighed stoichio-metrically and mixed homogeneously. Then, all of the raw materials were put into an agate mortar and then were ground for 30 min to make them fully mixed. Alumina crucible and alumina support were employed for high-temperature synthesis. After that, the samples were pre-fired at 1000 °C for 5 h and ground again for 30 min, then were sintered at different temperatures for 8 h in air. Finally, after cooling down to room temperature (RT) naturally, $ZnAl_2O_4$ and $Zn_{1-x}Al_2O_4$ phosphors were obtained for further measurement.

2.2. Fabrication of the LED device

The LED device was prepared by coating the near infrared phosphor on LED chip. Firstly, the phosphor was mixed with epoxy resin and curing agent with a mass ratio of 1:5:1. After stirring for 15 minutes, the prepared mixture was uniformly coated on the 285 nm LED chip, dried in an oven at 60 ^oC for 60 minutes, and then put in an oven at 135 ^oC for 80 minutes.

2.3. Characterization Techniques

X-ray diffractometry (XRD, Model SmartLab, Rigaku, Tokyo, Japan) was employed for phase identification, which was operated at 40kV/40mA using nickel-filtered Cu Kα radiation and the data was measured at a speed of 10.0° 2θ per minute, and the scanning range was 10°-70°. The XRD data for Rietveld refinement was gained through the step-scan mode, using a step interval of 0.02 and a counting time of 0.85 s per step. Rietveld refinement was performed using the TOPAS software. The X-ray photoelectron spectroscopy (XPS) data were obtained using X-ray photoelectron spectroscopy (Model Axis Supra, Kratos Analytical Ltd, Manchester, U.K.) under the monochromatic Al KαX-ray radiation of 1486.6 eV. The binding energies were calibrated by using C 1s (284.8 eV) of adventitious carbon as reference. The photoluminescence and persistent luminescence of $Zn_{1-x}Al_2O_4$ were detected using a JY FL3-21 spectrophotometer (HORIBA), and using a slit width of 10 nm in the kinetics mode. Diffuse reflectance spectra of the samples were obtained using a UV-Vis-NIR spectrophotometer (UV-3600 Plus, Shimadzu, Kyoto). Electron paramagnetic resonance (EPR) spectra were obtained using an EPR spectrometer (JES-FA 200, JEOL, Kyoto), and the frequency was 9.063 GHz.

2.4. Theoretical calculations

The first principle calculations are performed by using the Vienna ab initio simulation package [40,41]. The program has the projected enhancement wave pseudopotential [42] and the generalized gradient approximation of Perdew, Burke and Enzzerhof (PBE) exchange correlation functional [43], which is used to optimize the structure and obtain the free energy of all structures. The cutoff energy of the plane waves basis set is 500 eV and a Monkhorst-Pack mesh of 3×3×1 is used in K-sampling in the adsorption energy calculation and 7×7×1 is used in K-sampling in the density of state (DOS) calculation. In addition, van der Waals interactions corrected using DFT-D2 [44] are considered. The electronic self-consistent iteration is set to 10^{-5} eV, and the positions of all of the atoms are fully relaxed until the residual force on each atom is below 0.02 eV $Å^{-1}$.

3. Results and discussion

3.1. Synthesis and crystal structure of $Zn_{1-x}Al_2O_4$ (x=0-0.13)

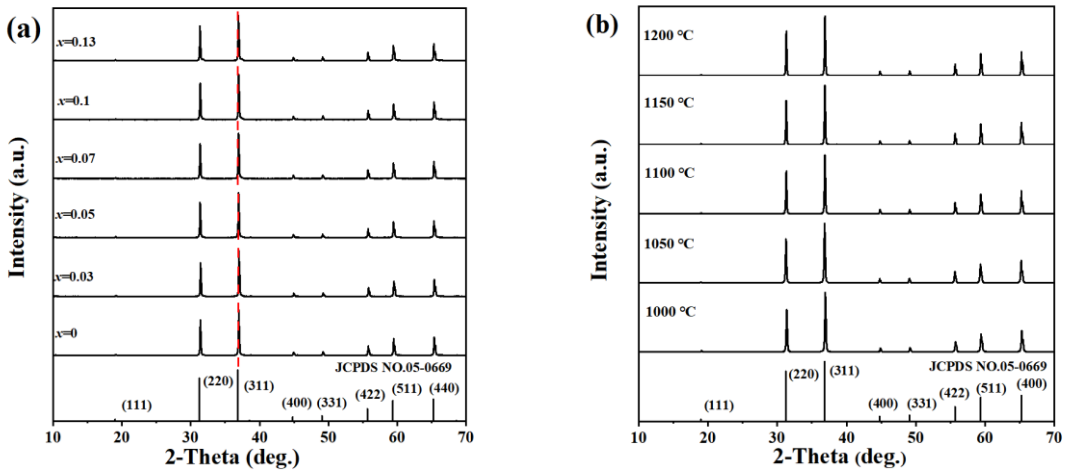

Fig. 1. XRD patterns of (a) $Zn_{1-x}Al_2O_4$ (x=0-0.13) calcined at 1500 °C and (b) $ZnAl_2O_4$ calcined at different temperatures.

Fig. 1a shows the X-ray diffraction patterns (XRD) of $Zn_{1-x}Al_2O_4$ (x=0-0.13) samples calcined at 1500 °C, while Fig. 1b shows the X-ray diffraction patterns (XRD) of $ZnAl_2O_4$ which sintered at different temperatures. The diffraction peaks saw in the XRD patterns of all $Zn_{1-x}Al_2O_4$ and $ZnAl_2O_4$ samples have a similar structure and in good agreement with the standard patterns of cubic spinel structure $ZnAl_2O_4$ (JCPDS No. 05-0669). The diffraction peaks of each sample are similar and can be well matched to (220), (311), (400), (331), (422), (511), (440) diffractions of $ZnAl_2O_4$. In addition, no trace of impurities was detected in $Zn_{1-x}Al_2O_4$ samples, through closely observation. The above results show that the zinc deficiency with the content of x=0-0.13 and the varied sintering temperatures do not significantly affect the crystal structure of $ZnAl_2O_4$. XPS survey spectra of $Zn_{0.87}Al_2O_4$ sample is shown in Fig. S1, and no other elements are detected in addition to the original components and contaminating carbon. The C1s peak at 284.8 eV from carbon contamination was used as a reference.

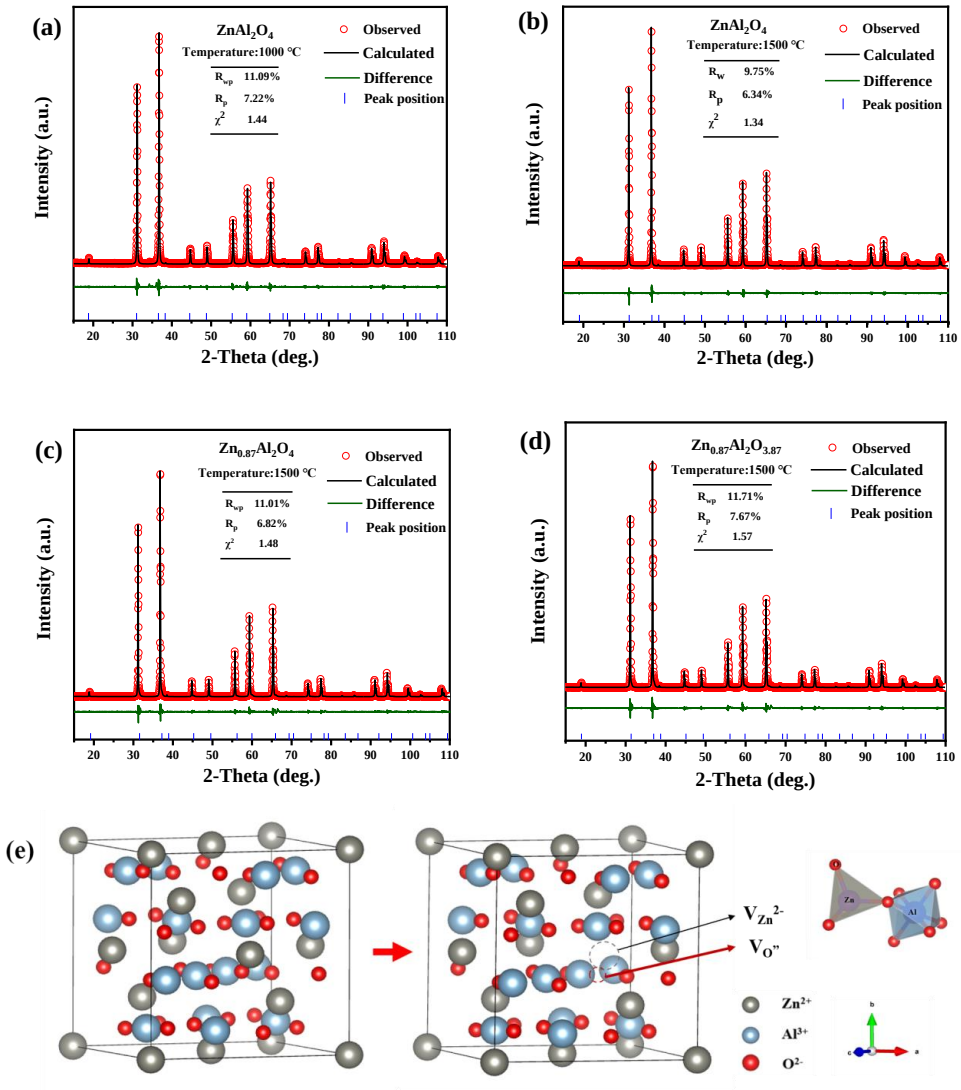

Fig. 2. Rietveld refinement analysis of XRD patterns for x=0 sample calcined at (a) 1000 ^{o}C and (b) 1500 ^{o}C, and (c, d) x=0.1 sample calcined at 1500 ^{o}C. (e) is the crystal structure for $ZnAl_2O_4$.

To further analyze the effect of zinc deficiency on the local structure of the spinels, the XRD Rietveld refinements for $Zn_{1-x}Al_2O_4$ samples with different zinc deficiency concentrations and $ZnAl_2O_4$ sample calcined at different temperatures are performed using the TOPAS software. The refinement results are shown in Fig. 2(a-d). The calculation results are consistent with the experimental data. The lattice parameters and the values of R_{wp}, R_p, and χ^2 are provided in the corresponding figures. The values of R_{wp}, R_p and χ^2 are quite low, suggesting that the results are credible. The structure of $ZnAl_2O_4$ spinel and its corresponding atomic positions (Table S1) are shown in Fig.

2e. In $ZnAl_2O_4$ crystal, Zn is coordinated with four oxygen atoms to form tetrahedron, and Al is coordinated with six oxygen atoms to form octahedron. ZnO_4 tetrahedron and AlO_6 octahedron are connected to each other by sharing O vertices and are evenly distributed in the unit cells of face centered cubic structure. When zinc is deficient in $ZnAl_2O_4$, zinc vacancy will appear, accompanied by the generation of oxygen vacancy. It is found that the lattice of ZAO shrinks in presence of Zn deficiency (Table S2).

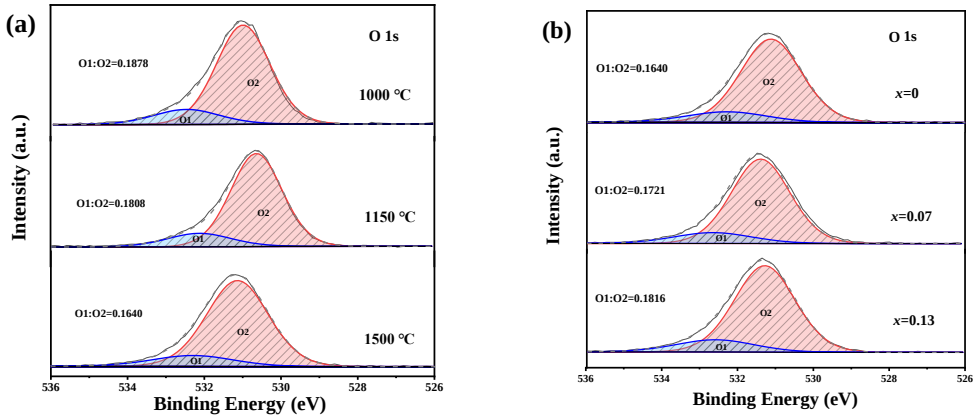

Fig. 3. XPS spectra of O1s for (a) $ZnAl_2O_4$ samples calcined at different temperatures, and (b) $Zn_{1-x}Al_2O_4$ (x=0-0.13) samples calcined at 1500 ^oC.

In order to verify the existence of oxygen vacancy, the XPS spectra of O1s were detected (Fig. 3). It is found that there are two peaks in the spectra of $ZnAl_2O_4$ (with different sintering temperatures) and $Zn_{1-x}Al_2O_4$ (x = 0, 0.07, 0.13). The former peak at 532.5 eV is attributed to adsorbed oxygen (O1) and the second peak at 531.3 eV is attributed to lattice oxygen (O2) [45,46]. The amount of adsorbed oxygen is closely related to the number of defects for oxygen vacancies. The number of oxygen vacancies can be determined indirectly by the amount of adsorbed oxygen. Therefore, the change of oxygen vacancy defect can be estimated through the peak intensity ratio of O1 and O2 corresponding the fitting peaks [30]. In Fig. 3a, with the increase of temperature, the ratio of O1 to O2 gradually decreases. Higher temperature makes the crystallinity be more perfect, and the intrinsic oxygen defects in the lattice decreases gradually. However, during the heating process, high temperature sintering will lead to a little loss of zinc, which leads to the increase of oxygen defects arising from charge balance. Because the zinc loss contributes to the appearance of oxygen defects

a little comparing with the decreased intrinsic oxygen defects, the total number of the oxygen defects decreases with the increase of temperature (Fig. 3a). However, for $Zn_{1-x}Al_2O_4$ sintered at 1500 °C (x=0-0.13, Fig. 3b), the ratio of O1 to O2 gradually increases with the increase of zinc deficiency concentration. When zinc is deficient in zinc aluminate, zinc vacancies appear in the crystal structure, which give rise to the appearance of oxygen vacancies for the charge balance. More oxygen vacancies arising from the decreased zinc content (x value) lead to a larger ratio of O1 to O2.

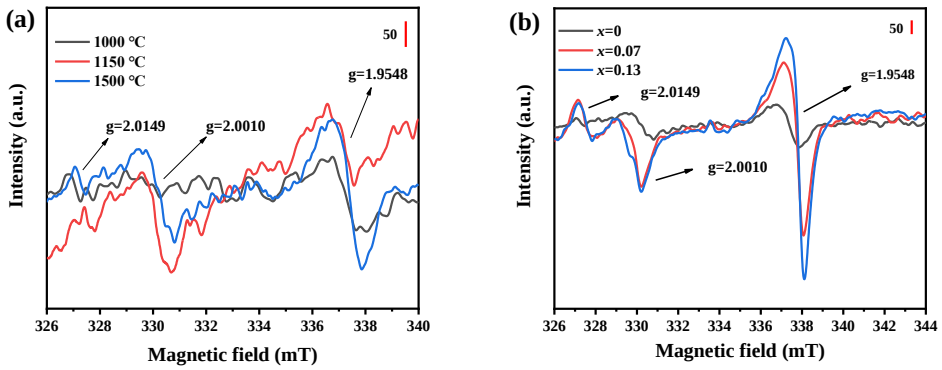

Fig. 4. EPR spectra for (a) $ZnAl_2O_4$ samples calcined at different temperatures and (b) $Zn_{1-x}Al_2O_4$ (x=0-0.13) calcined at 1500 °C.

The EPR spectra of $ZnAl_2O_4$ samples at different sintering temperatures and different zinc deficiency concentrations were measured to further clarify the number of oxygen vacancies (Fig. 4a and 4b). There are three different detection peaks in EPR spectra for all the samples, with the corresponding g values of 2.0149, 2.0010 and 1.9548, respectively. According to the reported works, the three values correspond to V_{Zn} (2.0149), V_O^{++} (2.0010), V_O^{+} (1.9548) defects respectively [47-50]. At different sintering temperatures, the EPR spectrum of $ZnAl_2O_4$ changes only in peak intensity, but not in the number of EPR signals in Fig. 4a, which indicates that there are three defects of V_{Zn}, V_O^{++}, and V_O^{+} in $ZnAl_2O_4$, and the types of defects do not change with the change of sintering temperature. With the increase of sintering temperature from 1000 to 1150 °C, the signal intensity becomes stronger, which confirms that the number of oxygen vacancy is gradually increasing. However, further increasing the temperature from 1150 to 1500 °C, the signal intensity becomes weaker. As

mentioned in the previous text, higher temperature makes the intrinsic oxygen defects decrease. However, high temperature sintering will also lead to the loss of zinc, which leads to the increase of oxygen defects arising from charge balance. Therefore, the above phenomenon is the comprehensive result from the variation of intrinsic oxygen defects and the oxygen defects arising from charge balance. Under the calcination condition of 1500 ^{o}C, it is found that the lack of zinc in $ZnAl_2O_4$ greatly improves the EPR signal intensity in Fig. 4b, and the signal peaks corresponding to the three types of vacancy defects are sharper and more intense compared with that in Fig. 4a. The signal intensity increases with the increase of zinc deficiency concentration. The EPR signal corresponding to g=1.9548 is attributed to V_O^+, which increases significantly with the increase of zinc deficiency concentration, indicating the increased amount of V_O^+. It can be conferred from the above results that the rapidly increased V_O^+ takes the dominate role on the increased oxygen vacancies.

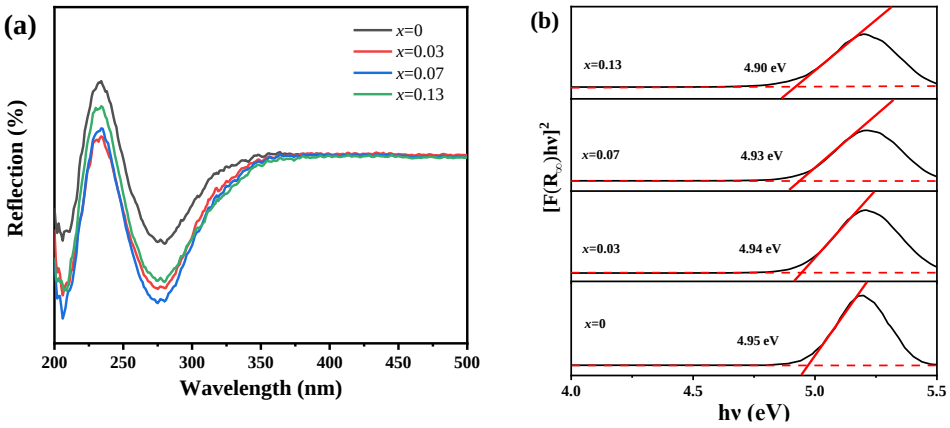

Fig. 5. (a) Reflectance spectra and (b) the band-gap energies for $Zn_{1-x}Al_2O_4$ (x=0-0.13) samples.

To estimate the optical band gap, the diffuse reflection (R_∞) of the $ZnAl_2O_4$ host was converted to the Kubelka−Munk function $F(R_\infty)$, and the formula is as follows [51]:

$$F(R_\infty)=S\times(1- R_\infty)^2/(2\times R_\infty) \quad \text{.....(1)}$$

As an approximate value, the diffusion coefficient S is independent on the wavelength. To reveal the possible influence of E_g, diffuse reflection spectra were recorded in Fig. 5a for the series of $Zn_{1-x}Al_2O_4$ (x=0-0.13), which were further

analyzed in Fig. 5b using the following equation [51,52]:

$$(h\nu \times F(R_\infty))^2 = A \times (h\nu - E_g) \quad (2)$$

Where A is a constant and $h\nu$ and E_g are the incident photon energy and the band-gap energy, respectively. Fig. 5b shows the values of the band gap energy for the samples with different zinc deficiency concentrations at 1500 °C, which can be read out from the intercept of the fitting straight lines. The results show that with the increase of zinc deficiency concentration (*x* value) from 0 to 0.13, the band gap energy decreases from 4.95 eV to 4.9 eV. The increase of zinc deficiency concentration will lead to more zinc vacancies and oxygen vacancies. The defect energy level of oxygen vacancy is below the bottom of conduction band, and the defect energy level of zinc vacancy is above the top of valence band. The defects of oxygen vacancies and zinc vacancies usually contribute to a little decrease of band gap energy [20].

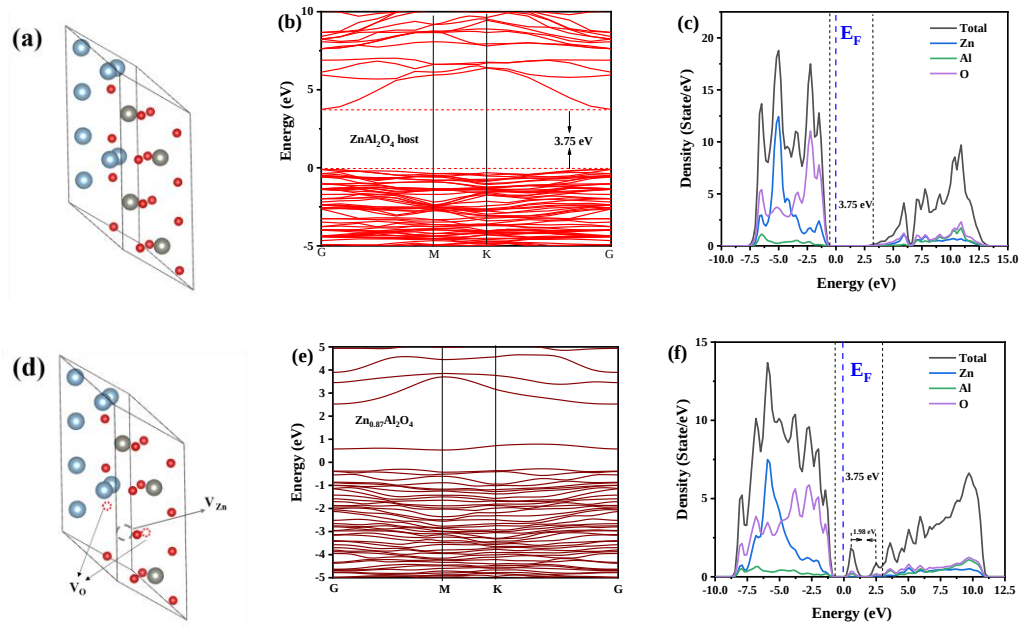

Fig. 6. Atomic distribution of the $ZnAl_2O_4$ host (a) and $Zn_{0.87}Al_2O_4$ (d). Electronic band structure (b and e) and the corresponding density of states (c and f) for the $ZnAl_2O_4$ host (b and c) and $Zn_{0.87}Al_2O_4$ (e and f).

In order to reveal the role of defects in luminescence behavior and clarify the location of defect energy levels, $ZnAl_2O_4$ host and $Zn_{0.87}Al_2O_4$ were calculated and analyzed by first principles. Fig. 6a shows the atomic distribution of $ZnAl_2O_4$. The

perfect $ZnAl_2O_4$ crystal has an indirect band gap (Fig. 6b) of about 3.75 eV, which is basically consistent with the reported $ZnAl_2O_4$ band gap (3.8 eV) [53]. This value is less than the experimental band gap (4.95 eV), because the calculated band structure is based on DFT method, which is insufficient description of exchange correlation. Then the density of states (DOS) of $ZnAl_2O_4$ is calculated, as shown in Fig. 6c. It is found that the energy level of oxygen vacancy defect exists below the bottom of conduction band, and which has also been proved by XPS (Fig. 3) and EPR (Fig. 4) analysis. The local atomic structure of $Zn_{0.87}Al_2O_4$ is shown in Fig. 6d. With the loss of Zn atoms, oxygen vacancy V_O is generated, the energy band structure and DOS of $Zn_{0.87}Al_2O_4$ are shown in Figs. 6e and 6f, and the band gap is 3.75 eV, which is similar to the perfect $ZnAl_2O_4$. However, there are two different trap bands in the band gap, with different depths (relative to the minimum conduction band) at 0.53 eV and 2.51 eV. According to the theoretical calculation, the two traps should be attributed to V_{Zn} and V_O respectively. The energy difference between the two defect levels is about 1.98 eV, which may possibly contribute to the NIR emission with the energy close to ~1.98 eV. Our previous work has found that defect energy levels could contribute to the near-infrared luminescence [30].

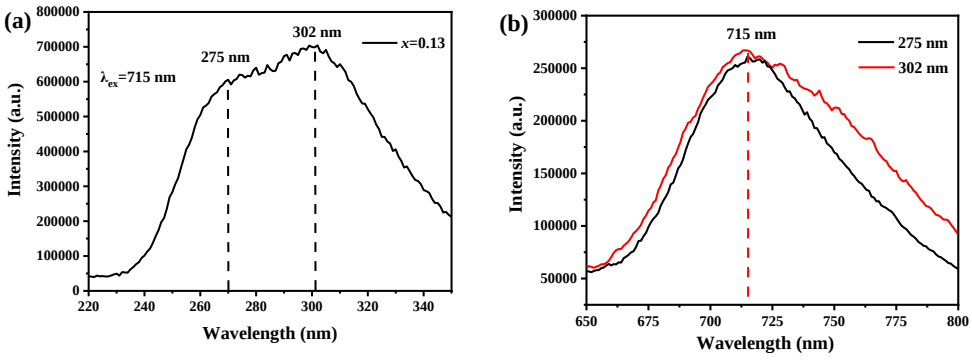

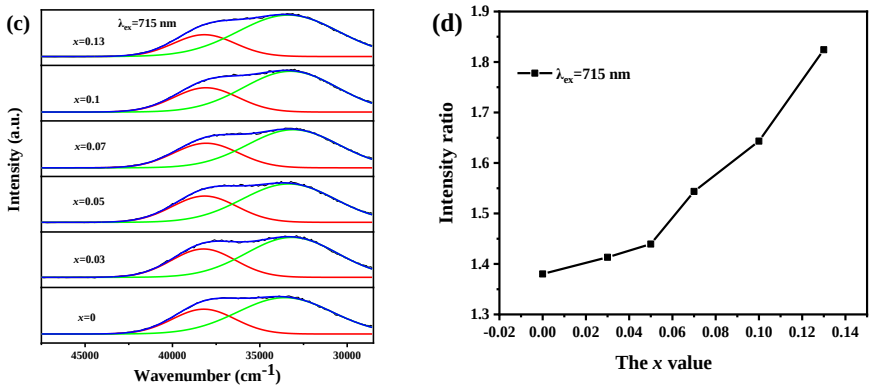

Fig. 7. (a) PLE and (b) PL spectra for x=0.13 sample at room temperature, (c) Gaussian fitting spectra and (d) intensity ratio for the PLE spectra of $Zn_{1-x}Al_2O_4$ (x=0-0.13) samples.

3.2. Photoluminescence, luminescence mechanism and application

In order to analyze the luminescence characteristics, the photoluminescence excitation (PLE) and photoluminescence (PL) spectra of the spinel phosphors were obtained. Fig. 7a shows the excitation spectrum (PLE) of $Zn_{1-x}Al_2O_4$ sample with zinc deficiency concentration of x=0.13 calcined at 1500 ^{o}C. It can be seen that the PLE spectrum exhibits an obvious wide excitation band under 715 nm monitoring, which contains two excitation peaks at 275 nm and 302 nm. The peak at 275 nm is due to the transition of the electrons from valence band to the oxygen vacancy level, while the peak at 302nm is due to the transition of the electrons from the zinc vacancy level to the oxygen vacancy level. Under the excitation of ultraviolet light at 275 nm and 302 nm, $Zn_{0.87}Al_2O_4$ both output a broad near-infrared emission band with the maximum at 715 nm in Fig. 7b. As can be seen in Fig. 7c, the PLE spectrum is fitted by Gaussian function. It is found that there are two excitation bands at 275 nm and 302 nm, and the intensity of 302 nm excitation band is higher. When the concentration of zinc deficiency increases gradually, the concentration of zinc vacancy also increases gradually, which results in more and more electrons being excited. When the samples are excited by 302 nm ultraviolet light, a larger number of electrons in the zinc vacancy level are excited to the oxygen vacancy level, which contributes to the stronger near-infrared luminescence. Therefore, the intensity ratio of I_{302} to I_{275}

gradually increases with the increase of zinc deficiency concentration in Fig. 7d.

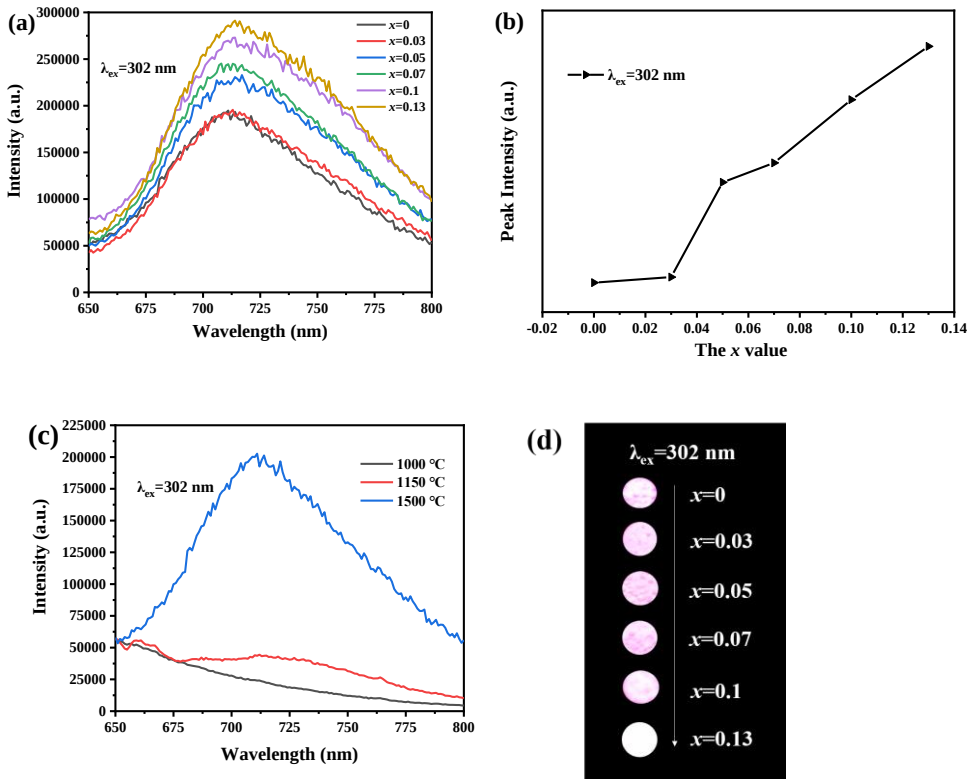

Fig. 8. (a) PL spectra and (b) relative NIR emission intensity for $Zn_{1-x}Al_2O_4$ (x=0-0.13) calcined at 1500 ºC and (c) PL spectra of $ZnAl_2O_4$ at different temperatures. (d) are the appearances of $Zn_{1-x}Al_2O_4$ (x=0-0.13) samples excited at 302 nm at room temperature, which are observed by night version device.

Fig. 8a shows the emission spectrum excited by ultraviolet light at the wavelength of 302 nm. The NIR emission intensity increases gradually with the increase of Zn deficiency concentration (Fig. 8b). In Fig. 8d, the near-infrared signals of $Zn_{1-x}Al_2O_4$ samples taken in the night vision mode under the excitation of ultraviolet light at 302 nm are observed. It can be found that their signal intensities are consistent with the emission spectra (Fig. 8a), and the x=0.13 sample emits brightest near-infrared light in night vision mode. However, no obvious NIR emission and weak NIR emission are found for the $ZnAl_2O_4$ samples calcined at 1000 ºC and 1150 ºC in Fig. 8c, respectively. Increasing the temperature from 1150 ºC to 1500 ºC yielded a considerable enhancement of NIR emission. The intrinsic oxygen defects may not contribute to the NIR emission, but the oxygen vacancy arising from the zinc loss is

closely related to the NIR emission. Although the number of oxygen vacancy decreases at a higher temperature, the oxygen vacancy arising from the zinc loss increases. Therefore, strong near-infrared light is observed for the sample calcined at 1500 ^{o}C (Fig. 8d). The lifetimes of the samples at 715 nm are about 2.8 ns (Fig. S2), which indicates that the lifetimes are not significantly affected by Zn deficiency.

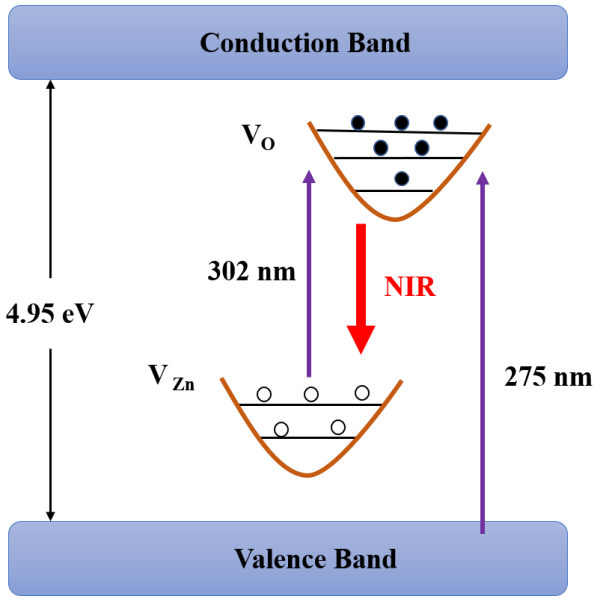

Fig. 9. Schematic representation of luminescence mechanism.

The luminescence mechanism of $ZnAl_2O_4$ was studied in Fig. 9, and the energy level diagram of $ZnAl_2O_4$ with Zn deficiency was constructed. The defect energy level below the conduction band is attributed to V_O defects, and the defect energy level above the valence band is attributed to V_{Zn} defects. Under the excitation at 275 nm, the electrons are excited from the valence band to the oxygen vacancy level. Because the zinc vacancy level is close to the Fermi level, which is full of electrons, under the excitation at 302 nm, the electrons are excited from the zinc vacancy level to the oxygen vacancy level. When the excited electrons are transferred from the oxygen vacancy level to the zinc vacancy level, broad near-infrared emission at 715 nm is found.

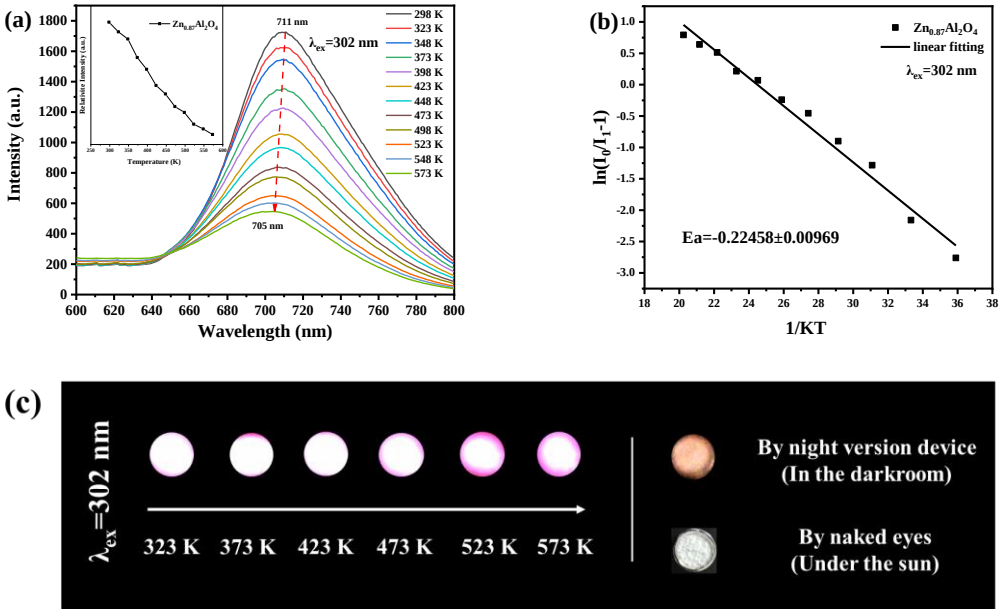

Fig. 10. (a) Temperature-dependent luminescence spectra excited at 302 nm, (b) ln (I_0/I_1-1) versus 1/KT plot for the determination of activation energy and (c) the appearances of $Zn_{0.87}Al_2O_4$ sample at different temperatures observed by night version device.

Fig. 10a shows the PL spectrum of $Zn_{0.87}Al_2O_4$ as a function of temperature under the excitation at 302 nm. When the temperature increases gradually, the molecular thermal motion increases gradually, and the crystal field intensity decreases, resulting in a large lattice shrinkage distortion and the decrease of Stokes displacement [54,55]. A blue shift of the emission peak from 711 nm to 705 nm was found by increasing the temperature from 298 K to 573 K, mainly due to the stokes displacement. The decrease of luminescence intensity with the increase of temperature is due to the enhancement of molecular thermal motion at high temperature, which intensifies the non radiative transition [55]. When the sample is excited by ultraviolet light, a large number of electrons are excited to the oxygen vacancy level. Then some electrons return from oxygen vacancy level to zinc vacancy level and contribute to the NIR emissions. However, some of the electrons are trapped by the oxygen vacancy. With the increase of heating temperature, although the luminescence intensity of the sample decreases gradually, the increase of temperature promotes the electrons release from the oxygen vacancy trap to compensate the emission loss. Therefore, when the

temperature rises to 100 °C, the luminous intensity of $Zn_{0.87}Al_2O_4$ still reaches 78.31%. After several times cycles of heating, the sample exhibited a good repeatability (Fig. S3). Combined with the corresponding fitting spectrum in Fig. 10b, it shows that the sample has good thermal stability, and the thermal activation energy is determined as Ea=-0.22458±0.00969 eV through the equation below:

$$A=\frac{A_0}{1+c\exp(-\frac{Ea}{kT})}$$

where A_0 and A are the integral area of the emission peaks at room temperature (298 K) and experimental temperature T, respectively, k is the Boltzmann constant (8.62 × 10^{-5} eV), and c is a constant.

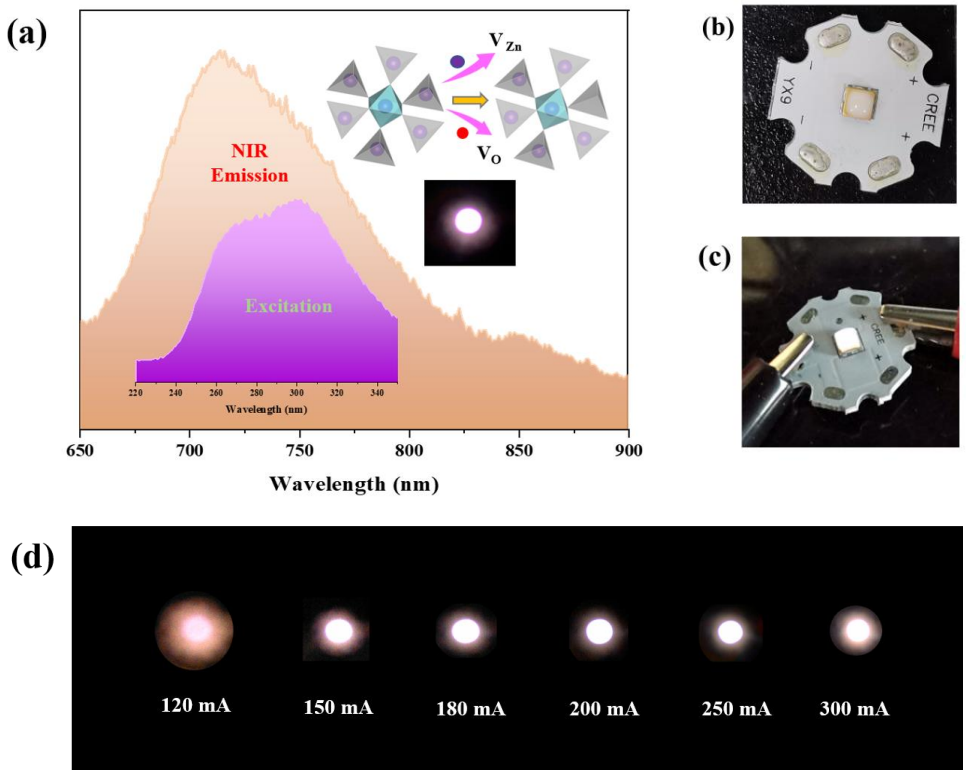

Fig. 11. (a) Schematic illustration for the near infrared LED and appearances of the LED lamp encapsulated by an ultraviolet LED chip and the $Zn_{0.87}Al_2O_4$ phosphor (b) not powered observed by naked eye and (c) powered observed by naked eye. (d) photographs and relative intensity of the fabricated LED under various currents (120-300 mA) observed by night vision instrument.

Fig. 10c shows the near-infrared emission of $Zn_{0.87}Al_2O_4$ at different temperatures

under the 302 nm real-time excitation. Through the observation of night vision instrument, there is not NIR afterglow in absence of UV light. However, the phosphor still exhibits intense NIR output with the temperature up to 125 ^{o}C. Further increasing the temperature to 175 ^{o}C resulted in the decrease of NIR signal. The results are consistent with the changes in temperature-dependent PL spectra.

Since the prepared phosphors can emit intense NIR emission under the UV light excitation, they are the candidate phosphors for NIR LED in Fig. 11a. As shown in Fig. 11, the LED lamp in Fig. 11b composed of $Zn_{0.87}Al_2O_4$ near-infrared phosphor and UV LED chip (285 nm) is powered on through the electroluminescent device. When the current is powered on, obvious near-infrared light in Fig. 11c can be observed through the night vision instrument. Even at a low current of 25 mA, the LED can show bright near-infrared light, and the luminous intensity increases with the increase of the driving current (show in Fig. 11d, e). Therefore, the NIR phosphors synthesized in this work have the prospect application in NIR LED.

4. Conclusion

A series of $Zn_{1-x}Al_2O_4$ (x=0-0.13) phosphors were synthesized by high temperature solid state reaction, which were characterized by a series of techniques, including XRD, UV-Vis, XPS, EPR, DFT calculation, PLE/PL spectroscopy, and temperature-dependent PL spectra analysis. The deficiency of zinc does not change the crystal structure of $ZnAl_2O_4$, but it results in the appearance of zinc vacancy (V_{Zn}) and oxygen vacancy (V_O). There are two kinds of oxygen vacancy, which are V_O^{++} and V_O^{+} in $ZnAl_2O_4$, with V_O^{+} taking the dominate role. The defects of oxygen vacancies and zinc vacancies contribute to the decreased band gap. Under the excitation of ultraviolet light at 302 nm, the $Zn_{1-x}Al_2O_4$ outputs a broad near-infrared emission band with the maximum at 715 nm, arising from the electron transition from oxygen vacancy energy level to zinc vacancy energy level. Higher concentration of zinc deficiency leads to stronger near-infrared luminescence. A blue shift of the emission peak from 711 nm to 705 nm was found by increasing the heating temperature from

298 K to 573 K, mainly due to stokes displacement. The sample exhibits a good thermal stability, because its luminous intensity remains 78.31% of that at room temperature with the heating temperature rising to 100 ^{o}C. Finally, the NIR phosphors have been successfully packaged on the UV LED chip (285 nm), which outputted bright and intense near-infrared light, indicating that the NIR phosphors synthesized in this work have the prospect application in NIR LED.

Acknowledgements

This work was supported in part by the Natural Science Foundation of Liaoning Province (Grant 2020-MS-081), and National Natural Science Foundation of China (Grant 51302032).

References and Notes

[1] J. Y. Shih, S. L. Lai, H. T. Cheng, Design and applications of LED textiles, Adv. Mater. Res. 821-822 (2013) 453-458.

[2] T. Pulli, T. Dönsberg, T. Poikonen, F. Manoocheri, P. Kärhä, E. Ikonen, Advantages of white LED lamps and new detector technology in photometry, Light: Sci. Appl. 4 (2015) e332.

[3] S. S. Kim, S. H. Cho, J. S. Yoo, S. H., Jo, J. D. Lee, Resistivity effect of $ZnGa_2O_4$:Mn phosphor screen on cathodoluminescence characteristics of field emission display, J. Vac. Sci. Technol., B: Microelectron. Nanometer Struct. 16 (1998) 2086-2090.

[4] C. H. Huang, Y. T. Cheng, Y. C. Tsao, X. K. Liu, H. C. Kuo, Micro-LED backlight module by deep reinforcement learning and micro-macro-hybrid environment control agent, Photonics Res. 10 (2022) 11.

[5] J. P. You, N. T. Tran, F. G. Shi, Light extraction enhanced white light-emitting diodes with multi-layered phosphor configuration, Opt. Express 18 (2010) 5055-5060.

[6] J. Y. Chen, C. F. Guo, Z. Yang, T. Li, J. Zhao, $Li_2SrSiO_4:Ce^{3+}$, Pr^{3+} phosphor with blue, red, and near-infrared emissions used for plant growth LED, J. Am. Ceram. Soc.

99 (2016) 218-225.

[7] B. Q. Zhao, Q. Zhu, X. D. Sun, J. G. Li, Co-doping Zn^{2+}/Sn^{4+} in $ZnGa_2O_4$:Cr^{3+} for dynamic near-infrared luminescence and advanced anti-counterfeiting, Ceram. Int. 47 (2021) 17000-17007.

[8] A. Bessière, S. Jacquart, K. Priolkar, A. Lecointre, B. Viana, D. Gourier, $ZnGa_2O_4$:Cr^{3+}: A new red long-lasting phosphor with high brightness, Opt. Express 19 (2011) 10131-10137.

[9] X. Y. Qu, Y. Hong, H. Cai, X. Sun, Q. Shen, D. L. Yang, X. C. Dong, A. H. Jiao, P.Chen, J. J. Shao, promoted intramolecular photoinduced-electron transfer for multi-mode imaging-guided cancer photothermal therapy, Rare Met. 41 (2021) 56-66.

[10] X. K. Zou, X. J. Wang, H. R. Zhang, Y. Y. Kang, X. Yang, X. J. Zhang, M. S. Molokeev, B. F. Lei, A highly efficient and suitable spectral profile Cr^{3+}-doped garnet near-infrared emitting phosphor for regulating photomorphogenesis of plants, Chem. Eng. J. 428 (2022) 132003.

[11] K. Pavani, J. S. Kumar, K. Srikanth, M. J. Soares, E. Pereira, A. J. Neves, M. P. F. Graca, Highly efficient upconversion of Er^{3+} in Yb^{3+} codoped non-cytotoxic strontium lanthanum aluminate phosphor for low temperature sensors, Sci. Rep. 7 (2017) 17646.

[12] R. P. Cao, X. G. Yu, X. Y. Sun, C. Y. Cao, J. R. Qiu, Near-infrared emission $Ba_3(PO_4)_2$:Mn^{5+} phosphor and potential application in vivo fluorescence imaging. spectrochim, Acta, Part A 128 (2014) 671-673.

[13] R. Peña, C. Algora, Evaluation of mismatch and non-uniform illumination losses in monolithically series-connected GaAs photovoltaic converters, Prog. Photovoltaics: Res. Appl. 11 (2003) 139-150.

[14] K. Oshima, K. Terasawa, S. Fuchi, Y. Takeda, Fabrication of wideband near-infrared phosphor by stacking Sm^{3+}-doped glass on Pr^{3+}-doped glass phosphors, Phys. Status Solidi C 9 (2012) 2340-2343.

[15] S. Fuchi, Y. Shimizu, K. Watanabe, H. Uemura, Y. Takeda, Ultrawide-band near-infrared light source over 1 mW by Sm^{3+}, Pr^{3+}-codoped glass phosphor combined with LED, Appl. Phys. Express 7 (2014) 072601.

[16] W. B. Dai, Y. F. Lei, J. Zhou, M. Xu, L. L. Chu, L. Li, P. Zhao, Z. H. Zhang,

Near-infrared quantum-cutting and long-persistent phosphor $Ca_3Ga_2Ge_3O_{12}$: Pr^{3+}, Yb^{3+} for application in vivo bioimaging and dye-sensitized solar cells, J. Alloys Compd. 726 (2017) 230-239.

[17] L. Yao, Q. Y. Shao, X. X. Xu, Y. Dong, C. Liang, J. H. He, J. Q. Jiang, broadband emission of single-phase $Ca_3Sc_2Si_3O_{12}$:Cr^{3+}/Ln^{3+} (Ln = Nd, Yb, Ce) phosphors for novel solid-state light sources with visible to near-infrared light output, Ceram. Int. 45 (2019) 14249-14255.

[18] Y. Zhang, R. Huang, H. L. Li, D. J. Hou, Z. X. Lin, J. Song, Y. Z. Guo, H. H. Lin, C.Song, Z. W. Lin, J. Robertson, Germanium substitution endowing Cr^{3+}-doped zinc aluminate phosphors with bright and super-long near-infrared persistent luminescence, Acta 155 (2018) 214-221.

[19] E. T. Basore, W. G. Xiao, X. F. Liu, J. H. Wu, J. R. Qiu, Broadband near-infrared garnet phosphors with near-unity internal quantum efficiency, Adv. Opt. Mater. 8 (2020) 2000296.

[20] J. Q. Xiahou, Q. Zhu, L. Zhu, S. Huang, T. Zhang, X. D. Sun, J. G. Li, Lattice-site engineering in $ZnGa_2O_4$:Cr^{3+} through Li^+ doping for dynamic luminescence and advanced optical anti-counterfeiting, J. Mater. Chem. C 10 (2022) 7935-7948.

[21] X. Xiang, G. K. Zhang, F. L. Yang, X. X. Peng, T. Tang, Y. Shi, X. L. Wang, An insight to the role of Cr in the process of intrinsic point defects in alpha-Al_2O_3, Phys. Chem. Chem. Phys. 18 (2016) 6734-6741.

[22] D. Gourier, A. Bessière, S. K. Sharma, L. Binet, B. Viana, N. Basavaraju, K. R. Priolkar, Origin of the visible light induced persistent luminescence of Cr^{3+}-doped zinc gallate, J. Phys. Chem. Solids 75 (2014) 826-837.

[23] Y. L. Wu, Y. Li, X. X. Qin, R. Chen, D. K. Wu, S. J. Liu, J. R. Qiu, Dual mode NIR long persistent phosphorescence and NIR-to-NIR stokes luminescence in $La_3Ga_5GeO_{14}$: Cr^{3+}, Nd^{3+} phosphor, J. Alloys Compd 649 (2015) 62-66.

[24] B. Liu, Y. H. Wang, Z. F. Wang, J. Zhou, X. L. Gao, Photoluminescence properties and degradation mechanisms of $BaMgAl_{10}O_{17}$:Eu^{2+} phosphor under baking treatment, Electrochem. Solid-State Lett. 13 (2010) J15.

[25] R. Singh, P. Kroll, Magnetism in graphene due to single-atom defects: dependence on the concentration and packing geometry of defects, J. Phys. Condens. Matter. 21 (2009) 196002.

[26] S. S. Lin, J. L. Huang, D. F. Lii, The effect of thickness on the properties of Ti-doped ZnO films by simultaneous r.f. and d.c. magnetron sputtering, Surf. and Coat. Technol. 190 (2005) 372-377.

[27] X. Tang, X. D. Li, Z. H. Zou, Z. D. Ma, J. C. Zhang, Z. F. Wang, Z. P. Ci, D. Y. Wang, S. L. Peng, H. H. Li, Y. H. Wang, A thermal-sensitizing and thermochromic phosphor, J. Mater. Chem. C 5 (2017) 10369-10374.

[28] X. Q. Yu, C. J. Summers, W. Park, Controlling energy transfer processes and engineering luminescence efficiencies with low dimensional doping, J. Appl. Phys. 111 (2012) 073524.

[29] N. Pathak, P. S. Ghosh, S. Saxena, D. Dutta, A. K. Yadav, D. Bhattacharyya, S. N. Jha, R. M. Kadam, Exploring defect-induced emission in $ZnAl_2O_4$: an exceptional color-tunable phosphor material with diverse lifetimes, Inorg. Chem. 57 (2018) 3963-3982.

[30] S. Y. Li, Q. Zhu, J. Q. Xiahou, J. G. Li, Doping Pb^{2+} in $LaAlO_3$ to generate dual emission centers and an optical storage container for visible and near infrared persistent luminescence, Dalton Trans. 51 (2022) 1112-1122.

[31] S. B. Roshni, M. T. Sebastian, K. P. Surendran, Can zinc aluminate-titania composite be an alternative for alumina as microelectronic substrate, Sci. Rep. 7 (2017) 40839.

[32] S. Sameera, V. Vidyadharan, S. Sasidharan, K. G. Gopchandran, Nanostructured zinc aluminates: a promising material for cool roof coating, J. Sci.: Adv. Mater. Devices 4 (2019) 524-530.

[33] H. Dixit, N. Tandon, S. Cottenier, R. Saniz, D. Lamoen, B. Partoens, First-principles study of possible shallow donors in $ZnAl_2O_4$ spinel, Phys. Rev. B 87 (2013) 174101.

[34] N. Pathak, S. K. Gupta, K. Sanyal, M. Kumar, R. M. Kadam, V. Natarajan,

Photoluminescence and EPR studies on Fe^{3+} doped $ZnAl_2O_4$: an evidence for local site swapping of Fe^{3+} and formation of inverse and normal phase, Dalton Trans. 43 (2014) 9313-9323.

[35] S. Sommer, E. D. Bøjesen, H. Reardon, B. B. Iversen, Atomic scale design of spinel $ZnAl_2O_4$ nanocrystal synthesis, Cryst. Growth Des. 20 (2020) 1789-1799.

[36] D. Zhang, C. Z. Wang, Y. L. Liu, Q. Shi, W. J. Wang, Y. Zhai, Green and red photoluminescence from $ZnAl_2O_4$:Mn phosphors prepared by sol-gel method, J. Lumin. 132 (2012) 1529-1531.

[37] G. L. Yu, W. R. Wang, C. Jiang, Linear tunable NIR emission Via selective doping of Ni^{2+} ion into ZnX_2O_4 (X=Al, Ga, Cr) spinel matrix, Ceram. Int. 47 (2021) 17678-17683.

[38] V. Singh, R. P. S. Chakradhar, J. L. Rao, D. K. Kim, Characterization, EPR and luminescence studies of $ZnAl_2O_4$:Mn phosphors, J. Lumin. 128 (2008) 394-402.

[39] M. Jain, Manju, M. Kumar, H. H. Lee, S. O. Won, K. H. Chae, G. Gupta, A. Vij, A. Thakur, Thermally induced cation ordering in $ZnAl_2O_4$:Mg^{2+}, Fe^{3+} for sensing thermal history through photoluminescence, J. Mater. Sci. 56 (2021) 12111-12120.

[40] G. Kresse, J. Furthmüller, Efficiency of ab-initio total energy calculations for metals and semiconductors using a plane-wave basis Set, Comput. Mater. Sci. 6 (1996) 15-50.

[41] M. D. Segall, P. J. D. Lindan, M. J. Probert, C. J. Pickard, P. J. Hasnip, S. J. Clark, M. C. Payne, First-principles simulation: ideas, illustrations and the CASTEP code, J. Phys.: Condens. Matter 14 (2002) 2717-2744.

[42] P. E. Blöchl, Projector augmented-wave method, Phys. Rev. B: Condens. Matter 50 (1994) 17953-17979.

[43] P. P. John, K. Burke, M. Ernzerhof, Generalized gradient approximation made simple, Phys. Rev. Lett. 77 (1996) 3865-3868.

[44] S. Grimme, Semiempirical GGA-type density functional constructed with a long-range dispersion correction, J. Comput. Chem. 27 (2006) 1787-99.

[45] H. H. Wang, L. L. Zhang, C. Hu, X. K. Wang, L. Lyu, G. D. Sheng, enhanced

degradation of organic pollutants over cu-doped $LaAlO_3$ perovskite through heterogeneous fenton-like reactions, Chem. Eng. J. 332 (2018) 572-581.

[46] G. Lee, I. Kim, I. Yang, J. M. Ha, H. B. Na, J. C. Jung, Effects of the preparation method on the crystallinity and catalytic activity of $LaAlO_3$ perovskites for oxidative coupling of methane, Appl. Surf. Sci. 429 (2018) 55-61.

[47] N. Pathak, S. Saxena, R. M. Kadam, Defect mediated optical properties in $ZnAl_2O_4$ phosphor, AIP Conf. Proc. 1942 (2018) 120008.

[48] C. Zhang, J. Lin, Defect-related luminescent materials: synthesis, emission properties and applications, Chem. Soc. Rev. 41 (2012) 7938-7961.

[49] A. B. Djurišić, W. C. H. Choy, V. A. L. Roy, Y. H. Leung, C. Y. Kwong, K. W. Cheah, T. K. G. Rao, W. K. Chan, H. F. Lui, C. Surya, Photoluminescence and electron paramagnetic resonance of ZnO tetrapod structures, Adv. Funct. Mater. 14 (2004) 856-864.

[50] H. B. Zeng, G. T. Duan, Y. Li, S. K. Yang, X. X. Xu, W. P. Cai, Blue luminescence of ZnO nanoparticles based on Non-equilibrium processes: defect origins and emission controls, Adv. Funct. Mater. 20 (2010) 561-572.

[51] T. L. Yu, S. D. Shan, C. Y. Li, P. E., M. ASCE, Effects of ice-breaking nose shapes on drift ice impact forces, J. Cold Reg. Eng. 26 (2012) 16-27.

[52] A. E. Morales, E. S. Mora, U. Pal, Use of diffuse reflectance spectroscopy for optical characterization of un-supported nanostructures, Bol. Soc. Mex. Fis. 5 (2007) 18-22.

[53] S. K.Sampath, J. F. Cordaro, Optical properties of zinc aluminate, zinc gallate, and zinc aluminogallate spinels, J. Am. Ceram. Soc. 81 (1998) 649-654.

[54] Y. N. Zhou, W. D.Zhuang, Y. S. Hu, R. H. Liu, H. B. Xu, M. Y. Chen, Y. H. Liu, Y. F. Li, Y. L. Zheng, G. T. Chen, Cyan-green phosphor $(Lu_2M)(Al_4Si)O_{12}:Ce^{3+}$ for high-quality LED lamp: tunable photoluminescence properties and enhanced thermal stability, Inorg. Chem. 58 (2019) 1492-1500.

[55] Y. H. Guo, S. H. Zhou, X. K. Sun, X. D. Lao, H. L.Yuan, $BaAl_{12}O_{19}:Eu^{2+}$ phosphors: molten salt flux synthesis and blue emission with high color purity and excellently thermal stability, J. Lumin. 211 (2019) 271-275.